



Supporting Information

for *Adv. Mater. Technol.*, DOI: 10.1002/admt.202000383

Smart Thermally Actuating Textiles

*Vanessa Sanchez, Christopher J. Payne, Daniel J. Preston, Jonathan T. Alvarez, James C. Weaver, Asli T. Atalay, Mustafa Boyvat, Daniel M. Vogt, Robert J. Wood, George M. Whitesides, and Conor J. Walsh**

Supporting Information

Smart Thermally Actuating Textiles

Vanessa Sanchez[†], Christopher J. Payne[†], Daniel J. Preston, Jonathan T. Alvarez, James C. Weaver, Asli T. Atalay, Mustafa Boyvat, Daniel M. Vogt, Robert J. Wood, George M. Whitesides, and Conor J. Walsh*

[†]Indicates equal contribution.

*to whom correspondence should be addressed: walsh@harvard.seas.edu

1. Detailed Materials and Fabrication of STATs

1.1 Laser Fabrication Methods

Material patterning for smart thermally actuating textiles (STATs) was done using vector cutting on a laser cutter. All laser cutting was performed using a 60-Watt CO₂ laser (VLS 6.60, Universal Laser Systems) with the 2.0 lens. According to the manufacturer, this lens has a focal length of 50.8 mm, a focal spot size of approximately 0.13 mm, and a 2.54-mm depth of focus which define the width, w , of the zone of ablation. The width was measured to be approximately 200 μm with the system configuration in this work (Figure S1).

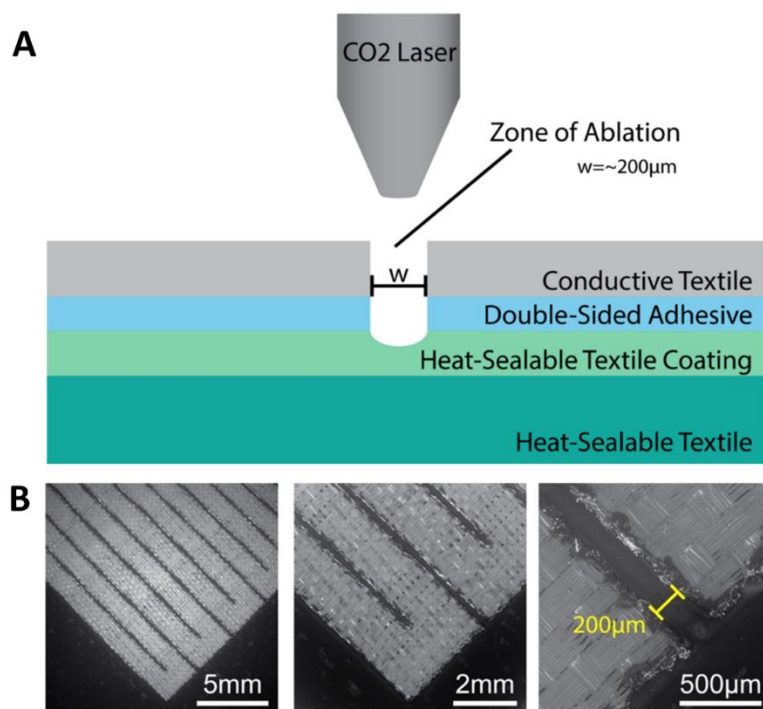


Figure S1. (A) Schematic and (B) SEM image indicating zone of ablation and width.

1.2 Textile Heater Fabrication

Joule heaters were incorporated on the interior of STATs. For the active heating material, woven silver-plated nylon (Shieldex Bremen Ripstop, V Technical Textiles Inc.) was adhered to a 5 μm double-sided adhesive (3M #82600 5 μm electronic double-sided tape, Bristol Tape Corporation). For the substrate material, a heat sealable woven textile coated with thermoplastic polyurethane (TPU) (1115 70D Nylon Taffeta with Single Coated Thermoplastic Polyurethane, Trelleborg) was taped to a flat surface with the coated side facing up for bonding. The conductive textile was then adhered to the coated side of the heat-sealable base textile, after which the sample was moved to the laser cutter bed. The heater pattern was cut with the laser at 15% power, 100% speed, and 900 pulses per inch (ppi) to cut the conductive textile and adhesive without cutting through the base substrate. An example of cut patterns is shown in Figure S2.

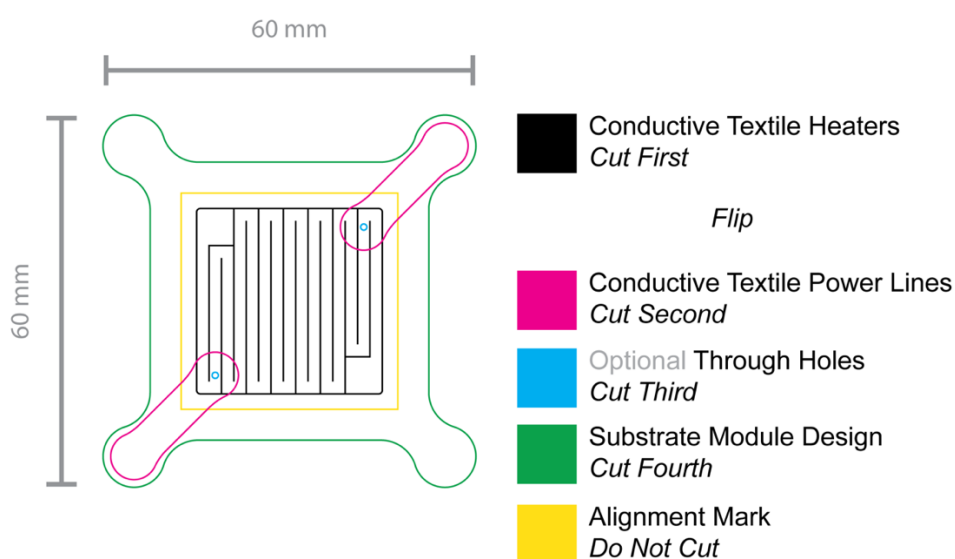


Figure S2. Laser cutter CAD and cutting process flow for a single modular STAT heater.

For fastener-based electrical connections and ports, 1 mm through holes were cut through all layers at laser settings of 75% power, 100% speed, and 1000 ppi. No through holes were cut for soft electrical connections.

After the laser cutting process, excess conductive textile was removed manually by peeling. To permanently adhere the conductive material to the substrate material, we thermally bonded the sample using a pressurized heat press (DK-20SP, Geo Knight & Co, Inc.) at settings of 170 $^{\circ}\text{C}$, 400 kPa, and 30 seconds. Fabrication processes can be viewed in Movie S1.

1.3 Textile Pressure Sensor Fabrication

Soft parallel plate capacitive pressure sensors consist of two conductive electrodes with a dielectric layer sandwiched between the electrodes. A process similar to heater fabrication was used to form the capacitor's base electrode and dielectric layer. For the capacitor's base electrode, woven silver-plated nylon was adhered to a 5 μm double-sided adhesive. For the substrate material, a heat sealable woven textile was cut and taped to a flat surface with the

coated side up for bonding. The sample was moved to the laser cutter bed. The conductive textile was then adhered to the coated side of the heat-sealable base textile. The desired electrode patterning was then cut with laser at 15% power, 100% target speed, and 900 ppi, allowing the conductive textile to be fully cut without cutting through the substrate. An example of cut patterns is shown in Figure S3.

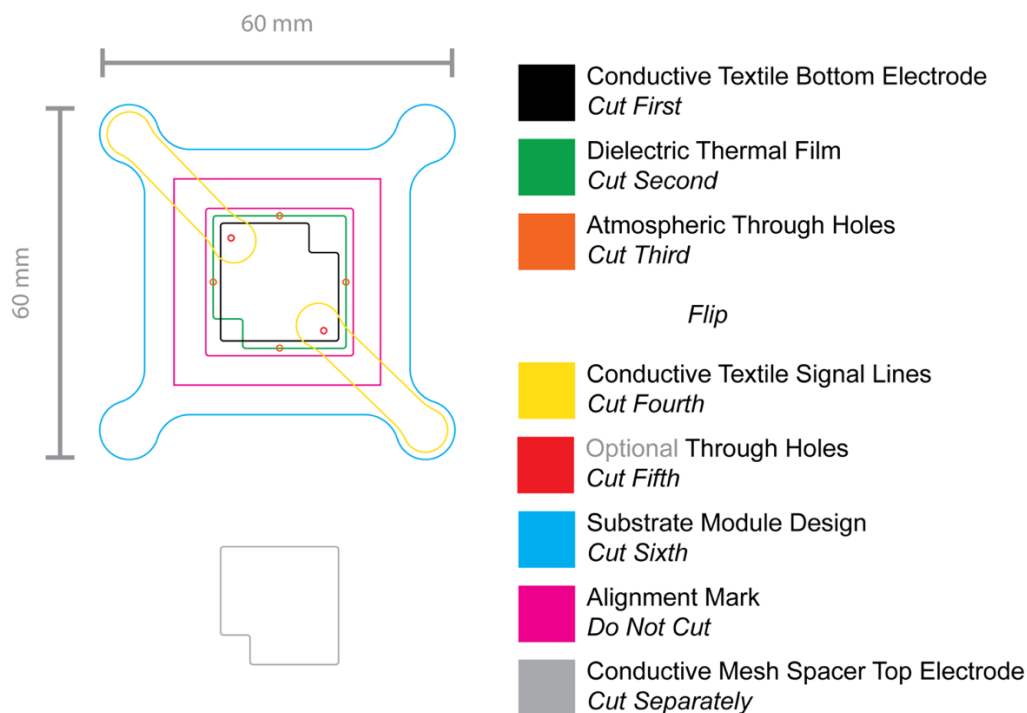


Figure S3. Laser cutter CAD design and cutting process flow for single modular STAT sensor.

Keeping the materials on the laser cutter bed and ensuring no movement to maintain alignment, we placed a dielectric layer comprised of a TPU film (3914 Sewfree Tape, Bemis Associates Inc.) pre-mounted to the 5 μm double sided adhesive upon the base electrode. We cut the dielectric layer using 20% power, 100% speed, and 900 ppi and removed excess material by manually peeling it away.

Through holes for atmospheric pressure regulation were then cut through all layers at laser settings of 75% power, 100% speed, and 1000 ppi. For fastener-based electrical connections and ports, 1 mm through holes were additionally cut through all layers at laser settings of 75% power, 100% speed, and 1000 ppi. No additional through holes were cut for soft electrical connections.

The patterned material was bonded thermally with a heat press at settings compatible with the heat sealable textile (170 $^{\circ}\text{C}$, 400 kPa, and 30 seconds). Immediately after removal, the mesh spacer textile (Shieldex Spacer B knit fabric, V Technical Textiles Inc.) electrode was manually aligned and placed atop, mesh side down (Movie S1) for bonding. This step was performed to prevent bonding of interior mesh to the dielectric when compressed by the heat press. Before the bonding step, this highly-compressible conductive mesh spacer textile

electrode was precut to shape using 8 passes of the laser at 75% power, 100% speed, and 1000 ppi. Fabrication processes are shown in Movie S1.

1.4 Power Line and Signal Line Fabrication

Integrated power and signal lines were incorporated on the exterior of STATs. Because the exterior is the non-coated side of the heat-sealable textile, an adhesive layer needed to be included. Thermal adhesive film was bonded to conductive woven silver-plated nylon using a pressurized heat press for 20 seconds at 150 °C and 400 kPa. The thermal film side of this laminate was then adhered to a 5 μm double-sided adhesive. This adhesive was used to attach the laminate to the uncoated side of the heat-sealable textile substrate.

The sample was then prepared for the active component (heater or sensor) following the relevant standard fabrication procedure described above with a modification. In this adaptation, the full textile sample was laser cut in an alignment rig for registration between the active component and the power or signal line. After we cut the active component in this rig, we flipped the material and placed it back into the rig to cut the power or signal lines. The cut file was designed to incorporate this flipping of material (Figures. S2, S3, S6-S8). The signal lines were cut via laser in the same alignment rig. We used laser settings of 24% power, 100% speed and 900 ppi to cut through the conductive textile and the thermal adhesive film.

For fastener-based electrical connections and ports, 1 mm through holes were cut through all layers, including the signal line, at laser settings of 85% power, 100% speed, and 1000 ppi. No through holes were cut for soft electrical connections. The sample was bonded thermally using a pneumatic heat press at settings designated for the substrate textile (170 °C, 400 kPa and 30 seconds).

1.5 Electrical Connection Fabrication

Electrical connections were formed to connect active components inside the STAT with their respective signal or power lines on the module exterior. We made fastener-based electrical connections by placing conductive fasteners in the precut through holes, described in the previous fabrication steps, and tightened the fasteners manually. Dual purpose conductive ports were made using vented M2 steel screws and nuts in place of fasteners. The ports were capped with M2 acorn nuts and instant adhesive.

Soft electrical connections were formed by shorting contact pads between layers by routing a conductive fiber (Liberator, Syscom Advanced Materials) through the thickness of all layers with a milliner's needle (JJ15003, John James). Conductive fiber ends were placed upon the contact pads. To maintain the electrical connection and seal the puncture hole for all connection points except for the mesh spacer electrode, we placed thermal adhesive film upon the contact pads and heat pressed using a pressurized heat press for 20 seconds at 150 °C and 400 kPa. To make connections at the mesh spacer electrode, we permanently adhered the layers by pressing with a sealing iron set to 170 °C for 5 seconds.

1.6 STAT Module Fabrication

To form a complete STAT module, heat sealable textiles with pressure sensors and heaters with pre-attached fastener-based or soft electrical connections and signal lines were layered with active components facing each other. Between the two active components, an additional layer of thin heat-sealable textile was sandwiched in the middle with its uncoated side facing the heater (labeled “membrane” in Figure 2C in the main text). The layers were sealed into complete modules by bonding the pouch edges using an impulse sealer (AIE 450-FD, American International Electric) set to level 6.5. This bonding process was repeated two times at each edge (once each per heater and sensor sides) so that each side would be sealed when placed next to the heating element of the impulse sealer.

As illustrated in Figure S4, STATs with fastener-based connections were filled with fluid after bonding all edges in an impulse sealer and fastening with an acorn nut. STATs with soft connections were filled by bonding the edge in in the syringe needle tip within one edge in the impulse sealer, connecting to the syringe, filling with fluid, and sealing once more.

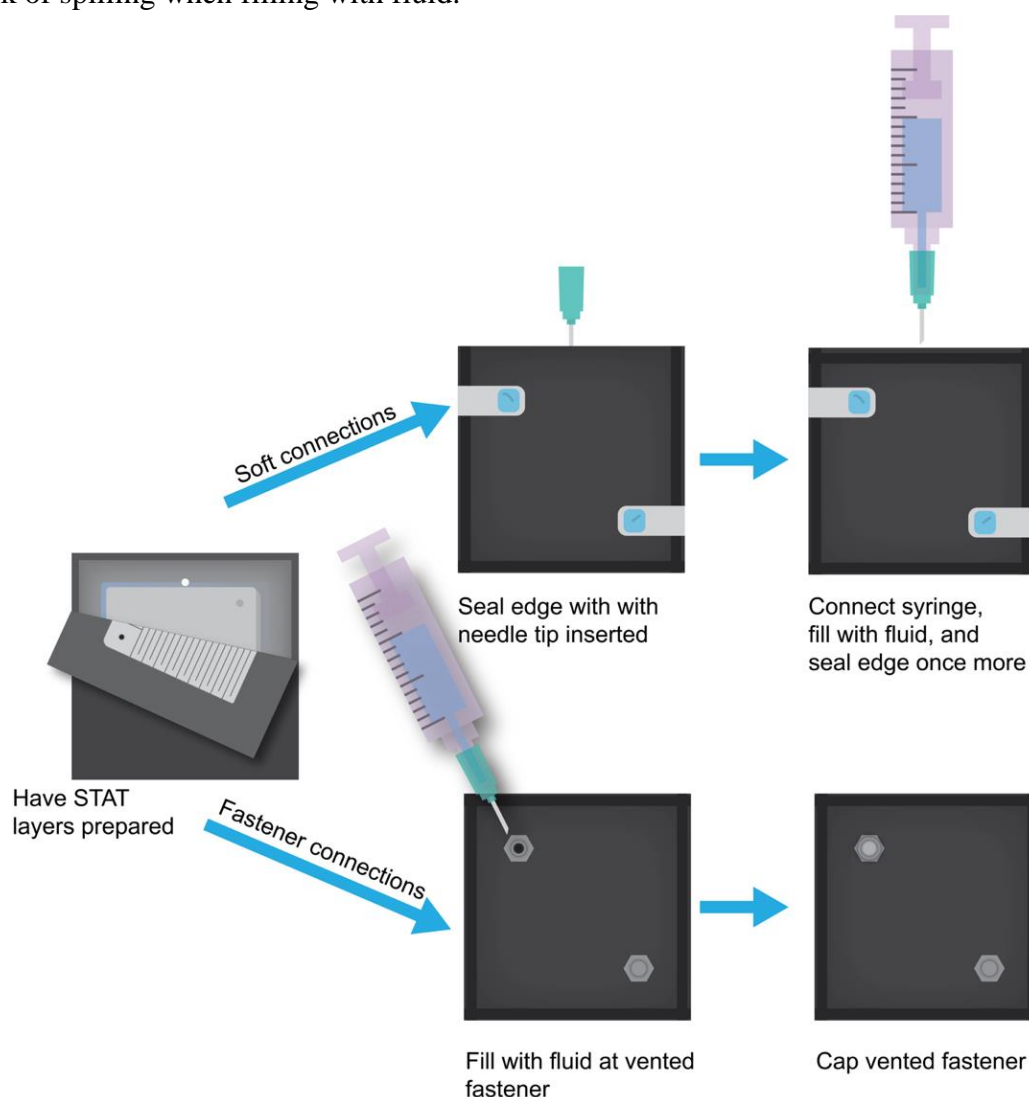


Figure S4. Fluid filling for STATs with soft connections and fastener-based connections

1.7 Magnetically Modular STAT Demonstration Fabrication

For modular STATs, magnetic connections were used for self-aligning attachments that require minimal user positioning (Figure 4A in the main text, Movie S2). To form this implementation of STATs, individual 15-line STAT modules with integrated power and signal lines were fabricated in the geometries seen in Figures S2 and S3, for heaters and sensors respectively, and sealed. To make the modular electrical and mechanical connections for the STAT heater and sensor, ring magnets (1/4" OD x 1/16" ID x 1/16" thickness Neodymium Rare Earth Ring Magnets, CMS Magnetics, Inc.) were then placed at each of the four corner tabs and sandwiched between the STAT and an additional exterior layer of conductive woven textile and sewn in place using a milliner's needle with conductive thread connecting all layers (Figure S5). To make a base textile for the STAT module to dock to, a ring of reflective thermal film (Reflectivedge, Bemis Associates Inc.), a disk of conductive knit textile (Shieldex Technik-tex P130+B, V Technical Textiles Inc.), an additional ring of thermal film (3914 Sewfree Tape, Bemis Associates Inc.), and a 1/4" ring magnet were layered on top of each other (Figure S5) and heat pressed for 20 seconds at 120 °C and 400 kPa onto a piece of warp knit textile (24710, Darlington). Conductive thread was sewn through all layers to act as a soft via, enabling an electrical connection to be made at the other side of the textile. 0.5 mL of Novec 7000 (Novec™ 7000, 3M Company) was injected into the module using a syringe, following the previously described process illustrated in Figure S4.

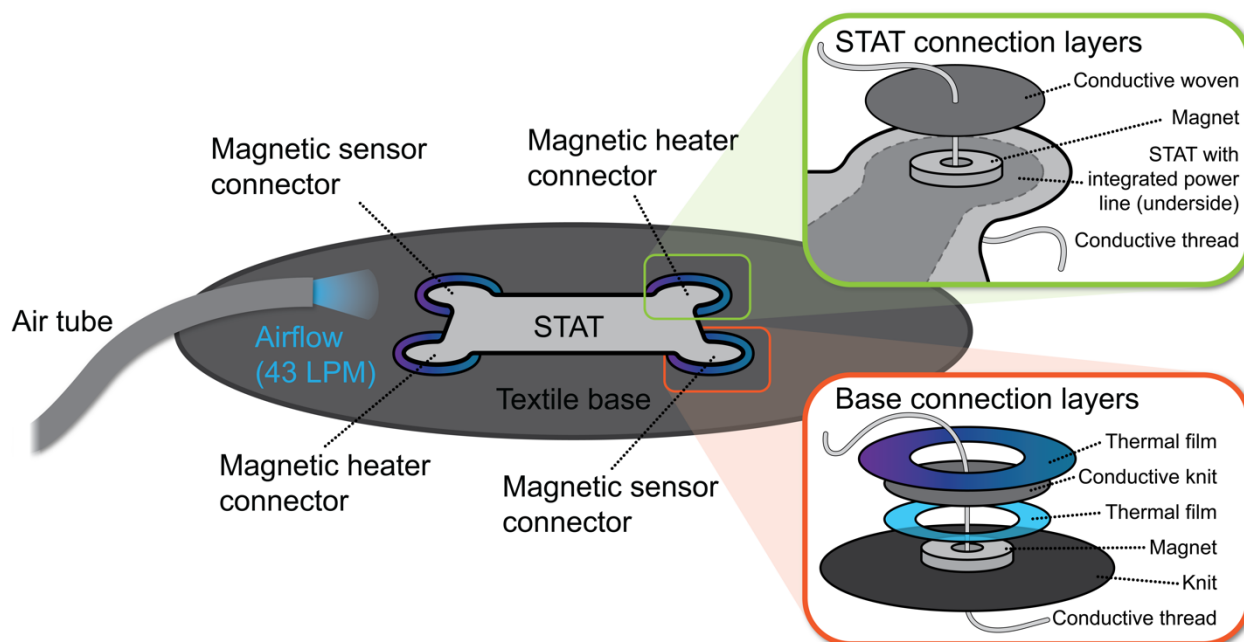


Figure S5. Experimental setup for modular STAT demonstration and airflow experiments. Insets show layers for modular magnetic connections for the STAT and the base textile dock.

1.8 STAT Array Demonstration Fabrication

3x3 STAT arrays were fabricated for the array demonstrations (Figure 4C in the main text, Movie S3) based on the laser cutting CAD diagrams shown in Figures S6 and S7. The sensors had soft connections, while the heaters had fastener-based connections with vented screws for ease of filling many STAT modules. 0.7 mL of Novec 7000 was injected into each module, and each module was then sealed mechanically.

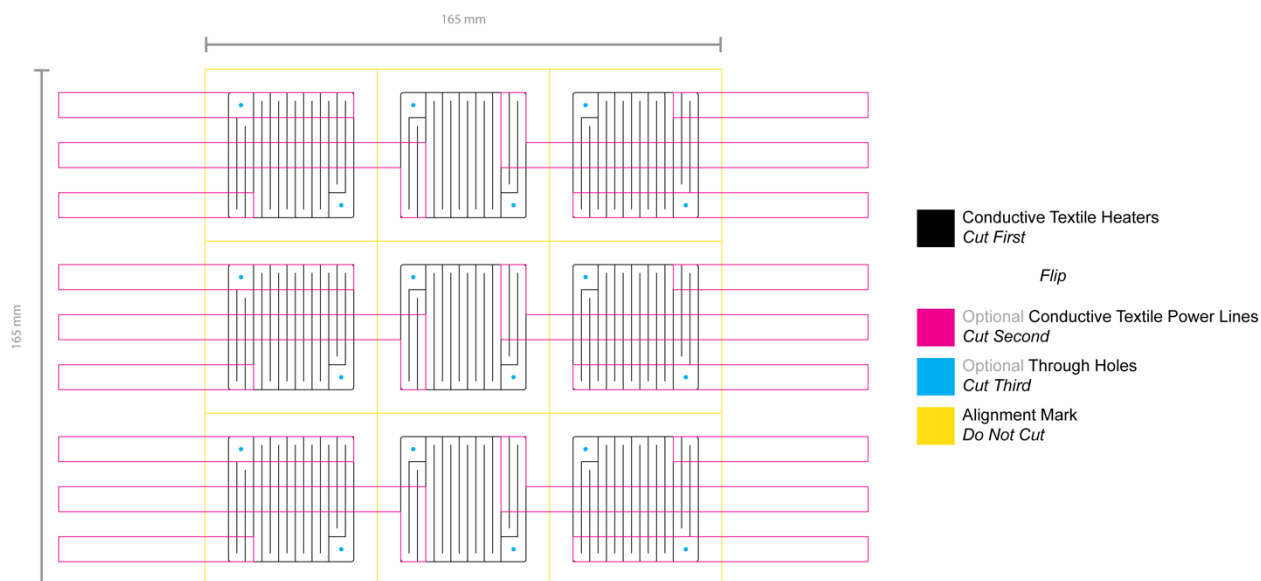


Figure S6. Schematic illustrating the laser cutter CAD geometry and cutting process flow for the 3x3 STAT heater array.

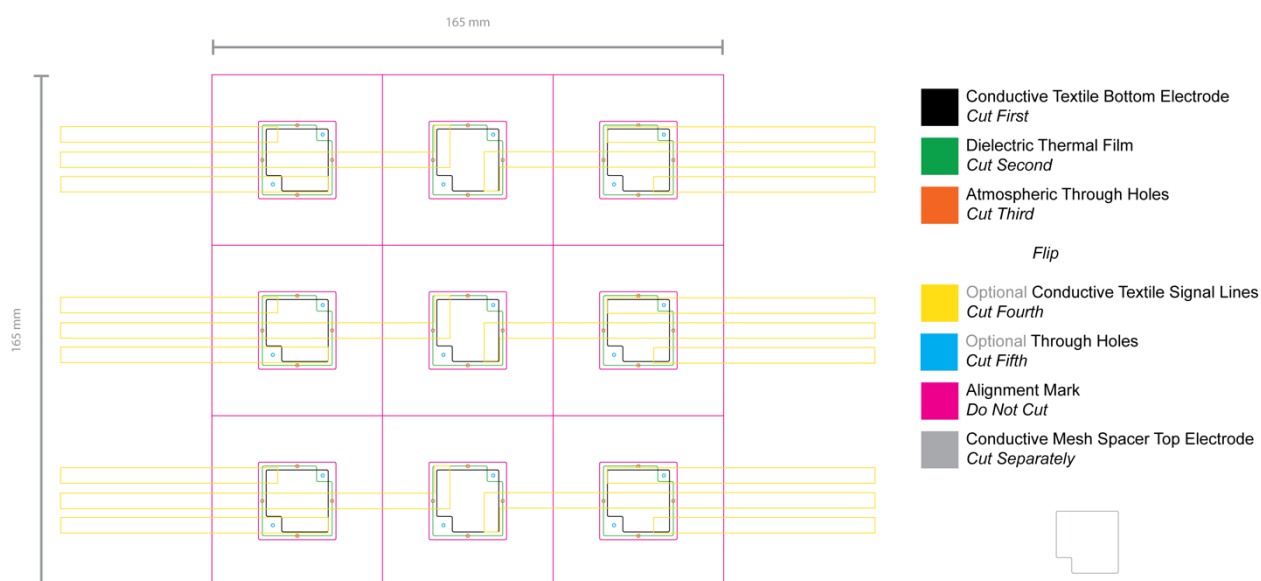


Figure S7. Schematic illustrating the laser cutter CAD geometry and cutting process flow for the 3x3 STAT sensor array.

1.9 STAT Artificial Muscle Demonstration Fabrication

A 5x1 array was fabricated for the artificial muscle demonstration (Figure 4C in the main text) based on the laser cutting CAD diagrams shown in Figure S8, with soft connections paired with integrated power lines at each heater. 0.5 mL of Novec 7000 was injected into each module, and each module was then sealed with an impulse sealer.

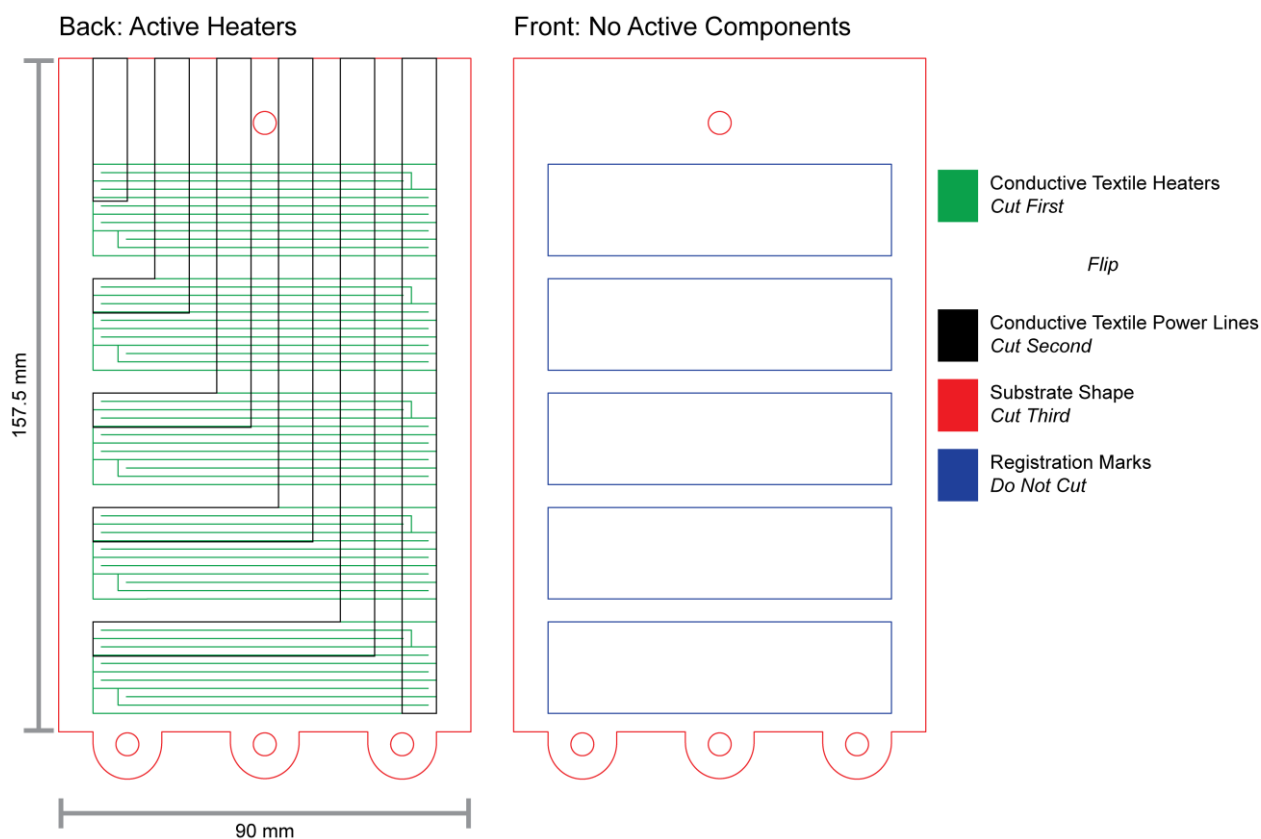


Figure S8. Laser cutter CAD design and cutting process flow for open-loop artificial muscle STAT actuator.

2. Modeling the Internal Pressure of STATs

2.1 Pressure-Volume Characterization

In order to model the internal pressure of STATs as a function of temperature (illustrated in Figure 3A in the main text), the material-dependent pressure-volume relationship needed to be characterized. This relationship was experimentally determined. Square-shaped (45 mm x 45 mm) inextensible actuator samples (made from two layers of Heat Sealable Coated Nylon Taffeta 70D) and extensible actuator samples (made from one layer of Heat Sealable Nylon Taffeta and one layer of heat sealable knit (DT8020, Eastex Products Inc.) were prepared. Samples did not incorporate integrated heaters or soft pressure sensors. Samples did incorporate an integrated 1/8" pneumatic line that was coupled to a 60 mL syringe and a pressure sensor (ADP5151, Panasonic) as shown in Figure S9. The output of the pressure sensor was monitored and recorded using a data acquisition system (USB-6218 BNC, National Instruments) connected to a computer.

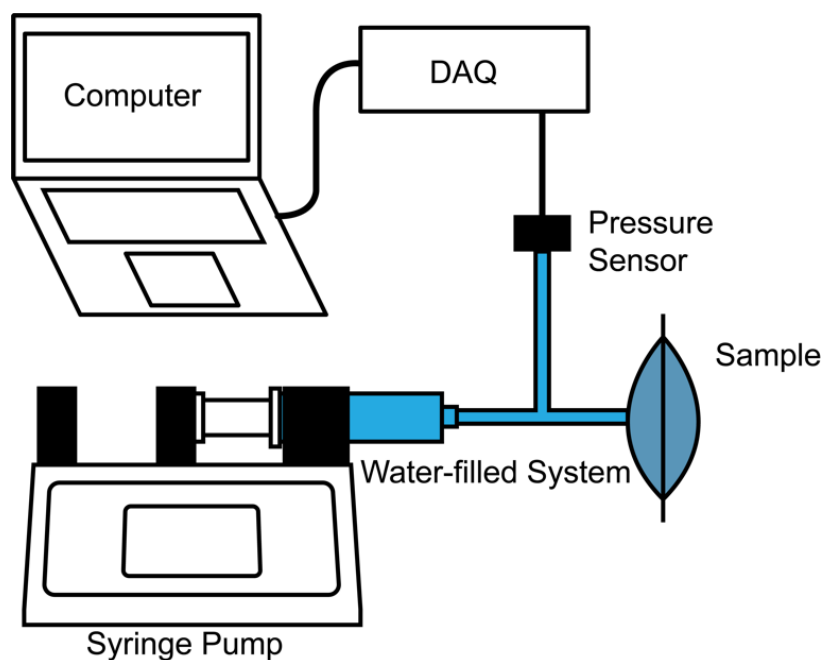


Figure S9. Experimental setup for the pocket pressure volume relationship.

The syringe was filled with water (used because it is approximately incompressible) and positioned in a syringe pump (PHD Ultra, Harvard Apparatus), which added and then removed fluid at a rate of 5 mL/minute. Inextensible samples were filled with 20 mL of water to prevent rupture at the increased pressures reached, while extensible samples were filled to 40 mL of water with pressure data continuously recorded. The ramp-up and ramp-down pressures were averaged to eliminate the flow-rate-dependent, additive contribution of the measured pressure due to fluid flow resistance through the pneumatic line connecting the syringe to the sample. The results are displayed in Figure S10.

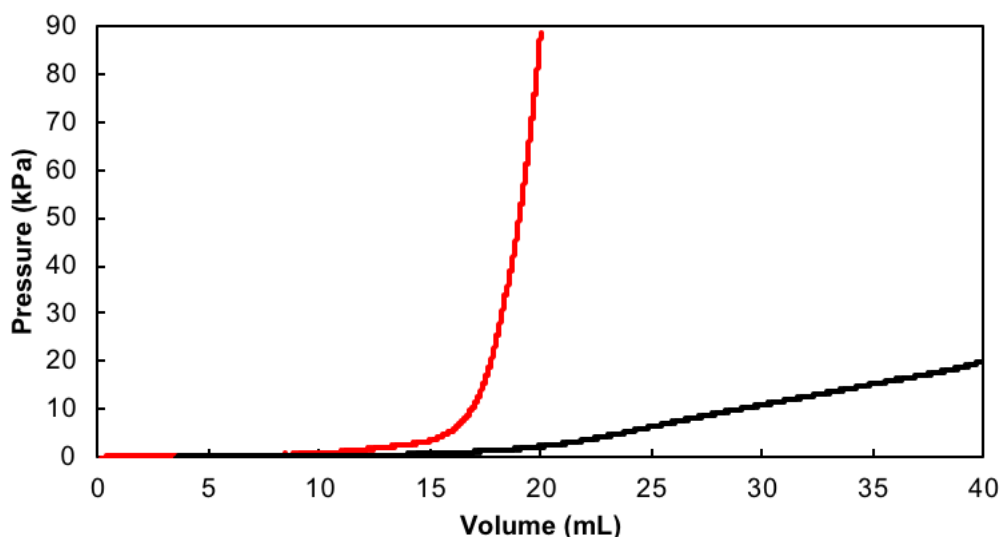


Figure S10. Pressure-volume relationship for inextensible sample (red) and inextensible/extensible sample (black).

2.2 Semi-Analytical Model for STAT Internal Pressure as a Function of Temperature

The internal pressure of a STAT as a function of its temperature was modeled by considering the dependence of the two fluids within the STAT—a saturated mixture of Novec 7000 liquid with its own vapor, and a small amount of residual air left inside from the filling process—on temperature. The total internal pressure, P_t , is the sum of the pressures of these two fluids:

$$P_t = P_n + P_a \quad (\text{S1})$$

where P_n is the pressure of the Novec 7000 vapor, and P_a is the pressure of the air (i.e., nitrogen, oxygen, etc.; fluids that exist only in the gas phase in the STAT). The pressure of the Novec 7000 is equal to its saturation pressure as long as a saturated mixture of both liquid and vapor exists within the STAT, which was the case for all of the experiments and demonstrations in this work; this saturation pressure is a function of temperature only.^[1]

$$P_n = \exp \left[\frac{-3548.6}{T} + 22.978 \right] \quad (\text{S2})$$

where T is the temperature of the Novec 7000 in units of K and P_n is the pressure of the Novec 7000 in units of Pa (absolute pressure). (Equation S2 yields the blue “pure Novec 7000 model” curve in Figure 3A in the main text, accompanied by experimental data for degassed—i.e., with a negligible amount of air—Novec 7000 in a rigid vessel.) Meanwhile, the pressure dependence of air on temperature is approximated by the ideal gas law:

$$P_a = \frac{nRT}{V} \quad (\text{S3})$$

where n is the number of moles of air inside of the STAT, R is the gas constant, and V is the internal volume of the STAT. The air and the Novec 7000 share the same volume, so $V_a = V_n = V$. The product nR is constant because the amount of air inside the STAT does not change during operation, and nR can be calculated at room temperature from Equations S3 and S4 if V is known. With $V = 2.5$ mL (which is the approximate volume of the STAT after filling), and with the total internal pressure at equilibrium with atmospheric pressure ($P_t = 101300$ Pa, yielding $P_a = P_t - P_n(T = 298 \text{ K}) = 38400$ Pa), nR is calculated as 0.000322 N-m/K. At this point, Equations S1-S3 could be combined to a single relationship between P_t , T , and V ; however, as evidenced in Figure S10, V is a function of P_t , and can therefore be substituted out. We fit an exponential to the data for the inextensible STAT (Figure S10) and found that the dependence of V on P_t is:

$$V = \frac{1}{660400} \ln \left(\frac{P_t - 101300}{0.1696} \right) \quad (\text{S4})$$

with an r^2 value of 0.9974 for the fit. Combining Equations S1-S4 results in:

$$P_t = \exp \left[\frac{-3548.6}{T} + 22.978 \right] + \frac{660400(nR)T}{\ln \left(\frac{P_t - 101300}{0.1696} \right)} \quad (\text{S5})$$

In Equation S5, P_t is a function of T , but also of itself, so we needed to apply a numerical approach to determine the value of P_t for a given T . In brief, we tested values of P_t ranging from 100000 to 800000 Pa, and then we chose the tested value of P_t that yielded the smallest error between the right- and left-hand sides of Equation S5. This process resulted in the red “Inext. textile model” curve in Figure 3A in the main text, which is accompanied by the experimental results measured for a STAT as described in the previous section.

As these modeling results highlight, the STAT exhibits a unique pressure-temperature dependence. Below the boiling point of Novec 7000, the actuator internal pressure balances with atmospheric pressure due to the presence of air within the actuator, combined with the relatively flat pressure-volume relationship in this regime (Figure S10) resulting from the soft, deformable nature of the textile walls; the internal pressure, composed of the additive pressures of this air and the Novec 7000 vapor, is essentially in mechanical equilibrium with the atmosphere below the boiling point because the volume can decrease until the pressure of the air compensates for the sub-atmospheric vapor pressure of the Novec 7000. Above the boiling point, however, the textile walls constrain expansion, and the internal pressure mirrors the saturation pressure of the Novec 7000, yielding a predictable, repeatable behavior across two regimes.

3. Textile Heater Design Guidelines

3.1 Textile Heater Resistance Characterization

Heater samples were produced using the methods described in Section 1, with several design parameters constrained to provide a general understanding of the resistive properties. First, non-conducting regions of the heater were minimized by making cuts into the conductive textile the size of the ablation width of the laser beam (200 μm , Figure S1). Second, a pattern where the pathway has a constant width (w) (Figure S11) was used. Third, the overall heater area was constrained to a 25 mm x 25 mm square (Figure S11A). Each heater thus had a fixed square area and the heating pathway could be divided into N number of lines, where N is an integer. For each heater design of a given N and w , there was a unique overall path length (L) such that the heater can occupy the entire heating element area. A wide range of heater element resistances can be achieved as the number of lines increases, since this methodology simultaneously reduces the width of the conductor whilst elongating the path length, which increases resistance.

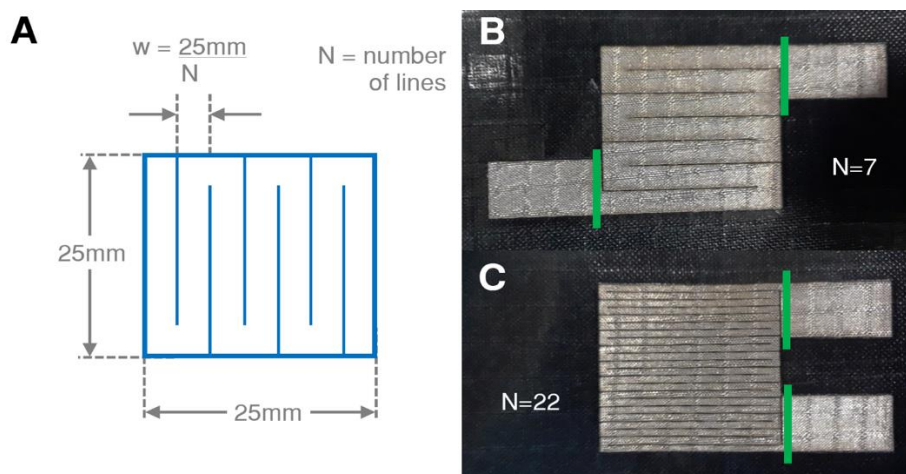


Figure S11. (A) Heater design with key dimensions and examples of (B) a heater with 7 lines and (C) a heater with 22 lines. Green marks indicate tabs where electrical connections are made for supplying current or measuring the resistance of a sample using a multimeter.

Heater samples were produced with number of lines spanning from $N = 3$ to $N = 25$. A total of 154 samples were fabricated (seven samples for each number of lines, N). Samples were loaded into a customized fixture where electrical connections were made at the corners of each heating element (Figures S11B-C, S12A). Electrical connections were made with 3 mm brass pins to minimize the effects of contact resistance, and a multimeter (Tek DMM 254, Tektronix) was used to measure the resistance of each sample. The fabrication of samples was spatially randomized to avoid systematic resistance errors resulting from variability in the conductive textile. Resistance measurements were logged, and mean averages were taken for each group of samples. The approximate resistivity of the conductive textile was calculated from the measured resistance and heater geometry. The heating element cross section was computed from knowledge of the element width ($(25 \text{ mm})/N$) and textile thickness ($76 \mu\text{m}$), where it is assumed the cross-section is rectangular. The path length calculation was based on the mid-line path length of the heating element.

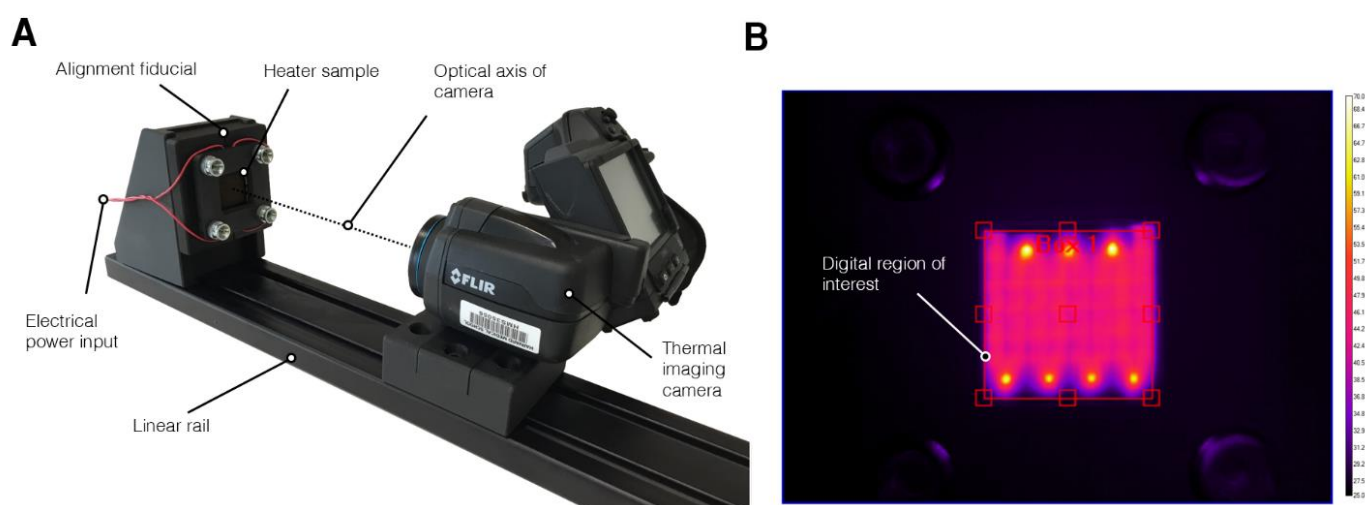


Figure S12. (A) Test rig for heater characterization studies and (B) a screenshot of the FLIR image processing software demonstrating the digital region of interest used to characterize the heater temperatures spatially and temporally (temperature scale bar ranges from 25 to 70 °C).

Figure S13 demonstrates that square resistive heating elements can be fabricated across approximately three orders of magnitude ($1.9 \Omega - 132.9 \Omega$). For all of the samples, the mean material resistivity was calculated to be $1.42 \times 10^{-5} \Omega\text{-m}$ (standard deviation = $1.14 \times 10^{-6} \Omega\text{-m}$) based on the measured resistance and geometry of each sample. Samples with a greater number of lines (longer element path length and shorter element width) had the greatest variability in overall resistance.

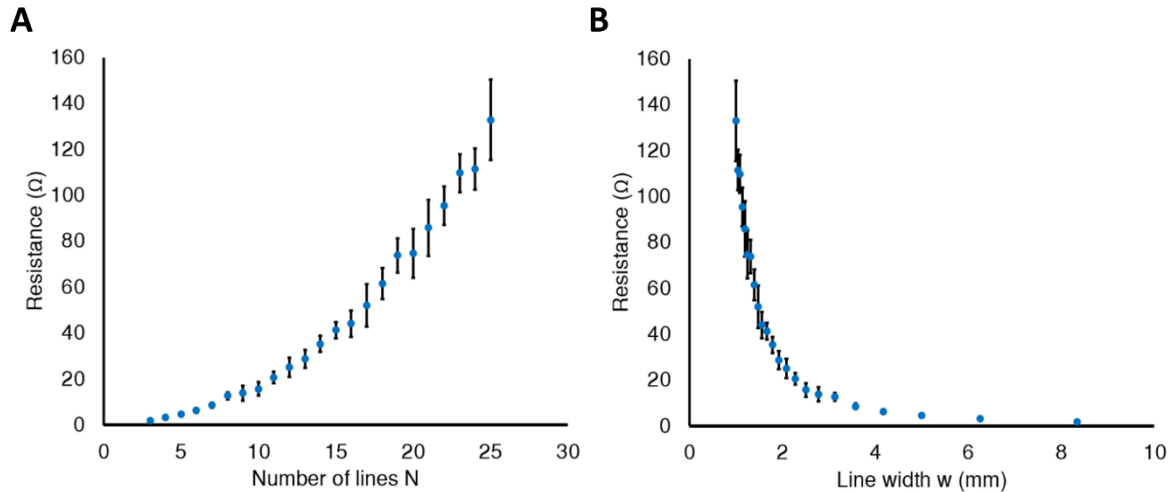


Figure S13. (A) Plot illustrating the relationship between heater sample resistance and the number of lines in the element design for square samples. Square joule heating elements can be fabricated across approximately three orders of magnitude ($1.9 - 132.9 \Omega$). (B) The same data represented in terms of the element line width. Data is based on seven samples for each group. Error bars indicate \pm standard deviation for each set of samples.

The effects of aspect ratio (AR) on heater resistance were subsequently tested. Again, non-conducting regions were minimized by using the ablation width from the laser beam ($\sim 200 \mu\text{m}$) as the separation between conductors to define the overall path, and a constant path width was used. A constant overall sample width (AW) was maintained and the path width (w) and path length were varied by changing N , the number of lines in the path. The heater had a fixed overall AR with its heating pathway divided into N number of lines, where N is an integer. For each heater design with fixed AR of a given N and w , there is a unique overall path length that occupies the entire heating element area. The path width (not accounting for material lost from ablation), w , was determined from the relationship between the overall area width (AW) and N :

$$w = \frac{AW}{N} \quad (\text{S6})$$

For example, in Figure S11A, where $AW=25 \text{ mm}$ and $N=7$, the schematic's path width can be determined as 3.57 mm.

Square samples where overall area width (AW) and overall area length (AL) were both set to 25 mm, varying N from $N=3$ through to $N=25$. A total of 154 square 25 x 25 mm samples

were fabricated (seven samples for each value of N). These square samples have an aspect ratio (AR) of 1, defined by the equation below:

$$AR = \frac{AL}{AW} \quad (S7)$$

In addition to the square samples, samples with varied aspect ratios and a constant area, where $AL \cdot AW = 625 \text{ mm}^2$ (equivalent to the area of the initial 25 x 25 mm square) were produced. To determine the dimensions of these samples, the following relationship was used:

$$AW = \sqrt{\frac{625 \text{ mm}^2}{AR}} \quad (S8)$$

$$AL = AR \cdot AW \quad (S9)$$

For the constant area, variable aspect ratio condition (dimensions in Table S1), samples with $AR = 2, 3,$ and 4 were produced. Within these AR sample sets, N was varied from $N = 5$ to $N = 25$, iterating by increments of 5, for a total of 105 samples. The fabricated samples were once more spatially randomized to avoid systematic resistance errors resulting from slight variability in the conductive textile.

Table S1. Dimensions of constant area, variable aspect ratio heater samples.

AR	AL [mm]	AW [mm]
2.0	35.36	17.68
3.0	43.30	14.43
4.0	50.00	12.50

Probes were connected at the two connection tabs (Figure S11 C-D), and a multimeter (Tek DMM 254, Tektronix) was used measure the total resistance of each heater sample. Resistance measurements were logged, and averages were taken for each group of samples.

3.2 Geometric Heater Resistance Model

As heaters of different shapes may be required based on the end application and the resistance will also need to be selected to accommodate the voltage source as well as differentiate heaters from power lines (as a similar-resistance power line will heat up along with the connected heater), we developed a simple geometric model to estimate the resistance of rectangular heaters of varying aspect ratios (AR) as described in equation S7. In our model, we first set the number of cuts, N_{cuts} :

$$N_{cuts} = N \quad (S10)$$

where N is the number of lines in the sample, so that the number of cuts accounts for all of the internal laser cut paths as well as half of the width of the laser cut path at the heater edge. We next take the path segment length, L_{path} , to be equal to the length of the total heater area, AL :

$$L_{path} = AL \quad (S11)$$

We then find the individual path segment width, W_{path} , accounting for the width of the material ablated away by the laser cut lines which is equal to N_{cuts} multiplied by the laser width, W_{laser} (referred to as “ w ” in Figure S1):

$$W_{path} = \frac{AW - N_{cuts} \cdot W_{laser}}{N} \quad (S12)$$

Using this path width along with the path length, we then obtain a path-specific aspect ratio, AR_{path} , for one path segment:

$$AR_{path} = \frac{L_{path}}{W_{path}} \quad (S13)$$

Because the average total path length is equivalent to adding the lengths of all path segments, by multiplying the path segment aspect ratio and number of lines by the sheet resistance of the conductive textile, SR , the resistance of the entire path, $pathR$, can be determined:

$$pathR = N \cdot AR_{path} \cdot SR \quad (S14)$$

We compared this path resistance model to the resistance measured from experimental samples of various aspect ratios and numbers of lines and saw good agreement (Figure S14). In the model predictions, we used 200 μm as the laser width and 0.165 Ω/sq as the sheet resistance.

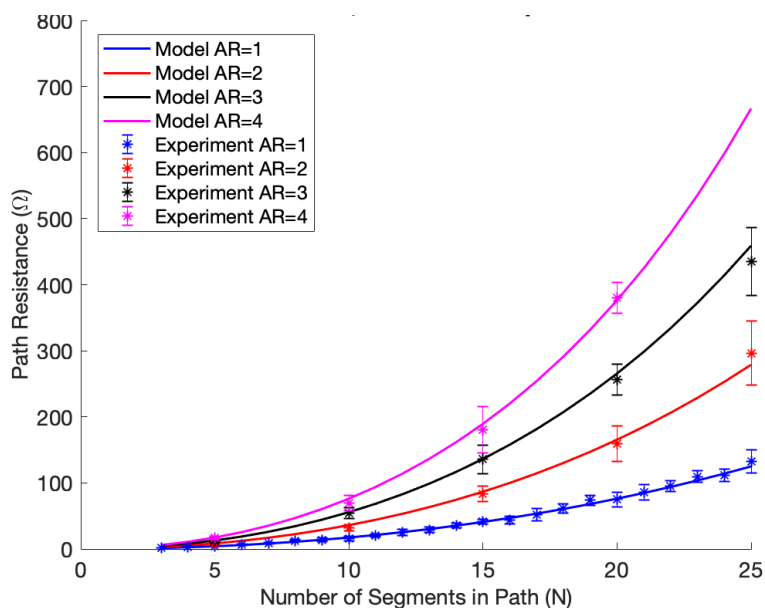


Figure S14. Plot illustrating the relationship between number of lines and total heater aspect ratio, and the geometric model used to estimate resistance.

3.3 Resistive Heater Thermal Characterization

To assess heater performance, we varied the conductive textile geometry to study the spatial surface temperature distribution and transient response of different heater designs in a free convection condition. Within 6 seconds, all heater samples could reach mean surface temperatures of around 70 °C (Figure S15). The 8-line heater design (lowest resistance, highest current) provided the fastest response time (72.1 °C at 6 seconds) and the 18-line design (highest resistance, lowest current) had the slowest response (69.3 °C at 6 seconds). The similarity in response time is largely expected due to equivalent power being dissipated over an equivalent area with equivalent heat transfer conditions. However, distinct differences in the spatial temperature distribution were observed between different heater designs (Figure 3B in the main text). Designs with more lines had more homogenous heating, with the majority of measured local temperatures close to the overall mean temperature of the heating area. The 8-line design had the greatest temperature heterogeneity, with hot spots forming on the corners of the conductive pathways and colder regions around the periphery of the heaters. Heterogeneous temperature distributions may impede device performance and reduce lifetime; conversely, a heater design that incorporates both hot and cold regions could have a faster or slower response time depending on where the low boiling point fluid is pooled.

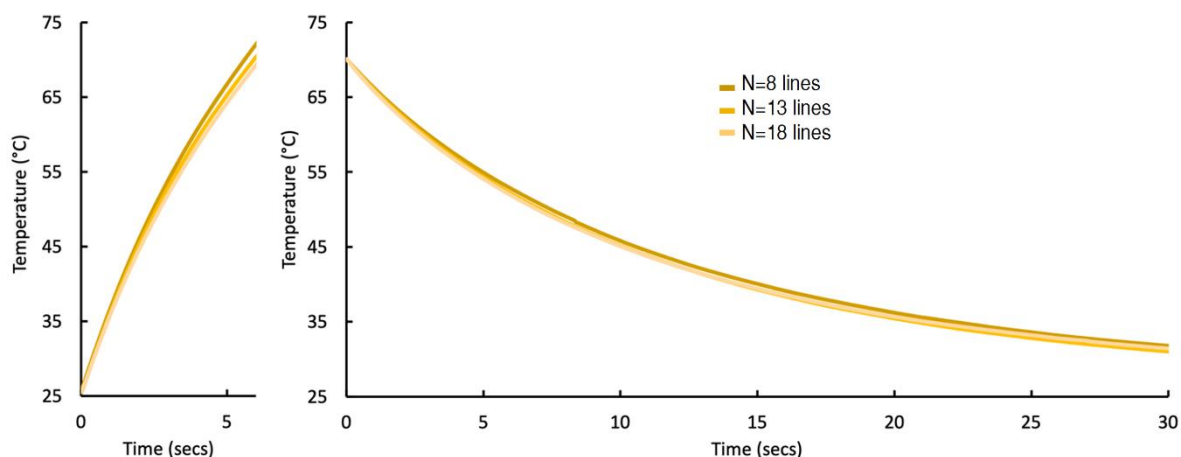


Figure S15. Temporal temperature response of different heater designs ($N = 8, 13,$ and 18 lines) when subjected to a 3 W power input (left), and related cooling curves for each design (right). Curves show a mean profile based on multiple samples for each heater design (seven samples for each heater design).

The higher resistance heaters have considerably lower overall temperatures, meaning that they are likely to have greater robustness and consistency over time. A drawback of the higher resistance heaters is the requirement for larger voltage inputs to achieve an equivalent power input to that of a lower resistance heater. High voltage requirements ($>15\text{ V}$) are less practical for many soft robotic applications (such as wearables), lack compatibility with off-the-shelf batteries, and introduce the risk of arcing between conductive traces.

An additional test was performed with a 13-line heater to quantify the temporal temperature distribution in heating and cooling (Figure S16), illustrating that the temporal distribution remains relatively heterogenous during the cooling phase. Power (3 W) was supplied for 7 seconds and the surface temperature captured using the methodologies previously described. Histograms were generated at 1 second, 3 seconds and 6 seconds after power was supplied. The sample was then allowed to cool, and a histogram was captured at 70 °C and at 5 and 20 seconds after this point. Corresponding thermal images were also captured to illustrate how the temperature distribution of a sample varies during these heating and cooling processes. Histograms were based on 0.5 °C intervals across a temperature range of $25\text{-}80\text{ °C}$.

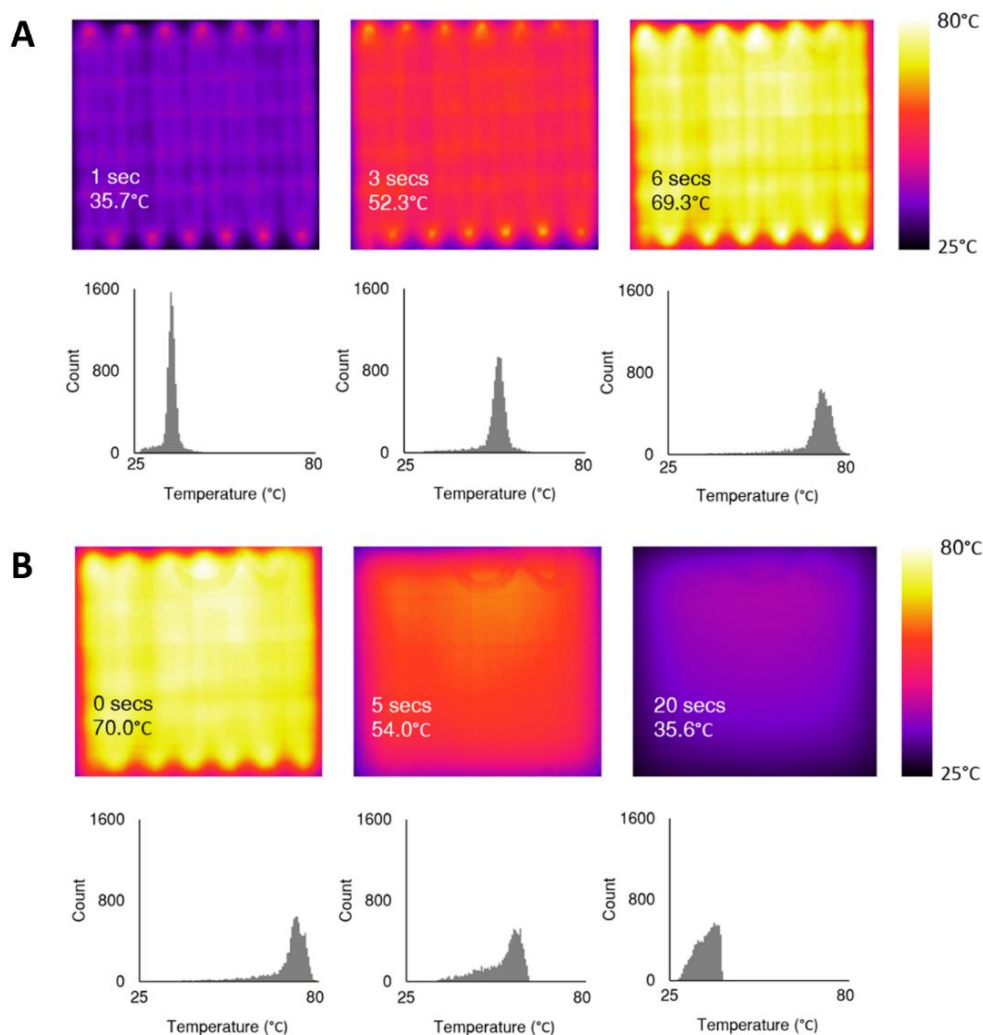


Figure S16. Temporal temperature response of a 13-line heater, with thermal images and corresponding histograms illustrating the temperature distribution. (A) heating process at 3 W at 1, 3, and 6 seconds after heater is powered on. (B) Cooling of heaters from 70 °C at 0, 5 and 20 seconds after heater is powered off in a free convection condition at an ambient temperature of 22 °C.

One limitation to this study is the requirement to image samples with the conductive material facing away from the camera. This step was necessary to avoid artefacts in the temperature measurements due to the disparate emissivity of the conductive textile heater material and base material. Consequently, the reported temperatures will be an underestimate of the surface temperature due to a temperature drop related to thermal conduction through the textile base. Furthermore, this methodology also captures some thermal diffusion which does not represent the exact temperature distribution on the surface of the conductive textile. These effects are nonetheless relatively small as the base textile is thin (~250 μm) and has negligible thermal mass. The effects are also systematic and apply to each tested sample.

Another limitation is that the observed temperatures represent a free convection condition on a sheet sample and do not fully represent the temperatures experienced within an integrated soft actuator. In reality, the temperature of the conductive textile will be considerably lower

due to the presence of the low boiling point fluid and boiling heat transfer that occurs during the actuation process. The test rig developed does, however, provide a controlled environment for reliably assessing differences in heater design as it is not practical to reliably quantify the surface temperature of a deforming actuator in three dimensions.

4. Open Loop Operation

4.1 Actuator Orientation Effects on Temporal Response

The effect of actuator orientation on temporal actuation response was studied using a 13-line actuator containing 0.5 mL of Novec 7000 (Figure S17). The actuator was mounted at 90° so that the heater plane was parallel to the direction of the gravity vector. Trials took place at an ambient room temperature of 22 °C. The device was repeatedly actuated at 3 W (over a course of seven trials), and mean transient profiles were generated.

The results demonstrated similar rates of pressurization for the pressure range of operation for this actuator (0-75 kPa) at a constant power input condition. Despite having a similar overall rate of pressurization, the pressurization profiles differed between orientations (Figure S17). The vertical orientation (heater parallel to gravity plane) demonstrated faster rates of pressurization in the first few seconds of actuation before slowing down, whereas in the horizontal orientation (heater perpendicular to gravity plane), the rate of pressurization accelerates. This result is most likely due to the fact the low boiling point fluid is initially guaranteed to be in direct contact with a region of the heater in the vertical orientation, whereas in the horizontal orientation, some of the working fluid may pool in the peripheral regions, hindering heat transfer in the initial stages. However, after the actuator begins to take up an inflated form, fluid in the peripheral region will pool in the central region of the heater due to gravitational effects, accelerating boiling heat transfer and fluid vaporization. Although the overall pressurization rate is relatively invariant to actuator orientation, the result nonetheless highlights how uncertainties in the state of the actuator alter its performance, motivating the requirement for sensory feedback to facilitate control and repeatable actuation of such devices. One limitation of this study was that testing could not be performed with the heater facing down (since fluid would collect in the pneumatic line connected to the pressure sensor in this condition). It is likely that heat transfer from the heater to the fluid would be considerably less efficient in this condition because the fluid would not be in direct contact with the heater. One possible solution for this would be to adopt heaters on both sides of the actuator to account for this uncertainty in future implementations. Another solution could be to incorporate a wicking material over all of the internal surfaces of the actuator to ensure a uniform distribution of fluid regardless of orientation.

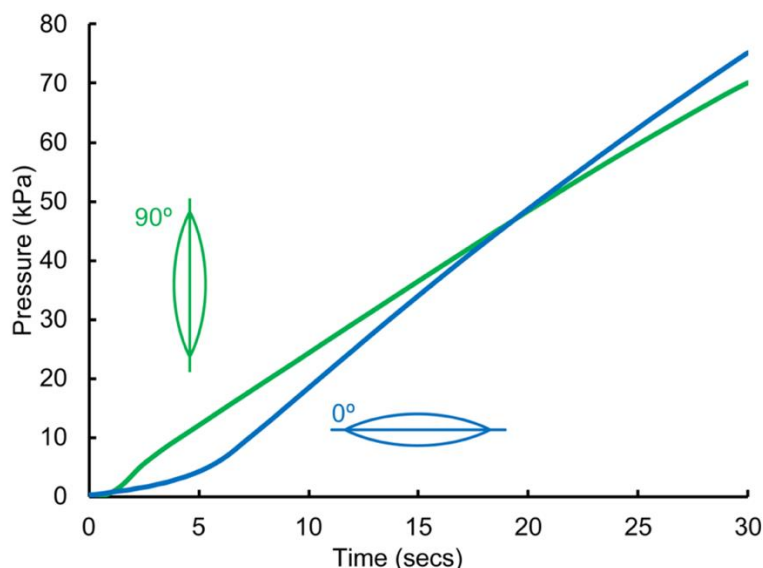


Figure S17. Effect of orientation on open loop pressurization profile data based on a 3 W power input to a 13-line heater sample (average profile based on six repeated measurements)

4.2 Steady-State Model for Pressure as a Function of Power during Open-Loop Operation

A steady-state open-loop thermal resistance network model was developed to characterize the sensitivity of the STAT to environmental conditions (Figure S18). Heat is introduced to the network at a constant rate, equal to the input electrical power, through the heater. Under steady-state conditions, the temperatures at each node of the network do not change over time, and no energy is added to (or removed from) each node; instead, all of the power input to the heater must leave the network through either the upper or lower faces of the STAT. Two cases were modeled: The STAT as an actuator surrounded by air on all sides (Figure S18(a)), and the STAT as a wearable adjacent to the human body (Figure S18(b)).

The lower pathway consists of thermal resistances for (i) conduction heat transfer through the fabric of the lower layer of the STAT pouch (R_{lower}) and (ii) either convective heat transfer from the outer face of the lower fabric to the surrounding air (R_{air}) in the case of the STAT in an air environment (Figure S18(a)), *or* conductive heat transfer through the skin to the human body (R_{skin}) in the case of the STAT as a wearable (Figure S18(b)). The upper pathway includes thermal resistances for (i) boiling the internal fluid (R_{boil}), (ii) recondensing the fluid on the interior of the upper fabric layer (R_{cond}), (iii) conduction heat transfer through the fabric of the upper layer of the STAT pouch (R_{upper}), and (iv) convective heat transfer from the outer face of the upper fabric to the surrounding air (R_{air}). Representative values for these thermal resistances, normalized for area, are presented in Table S2. The heat transfer coefficient of convection into air, h_{air} , is on the order of $50 \text{ W/m}^2\text{K}^{[2]}$ with a slight breeze.

The thermal conductivity of nylon fabrics ($k_{\text{upper}} = k_{\text{lower}}$) is 0.25 W/m-K , and their thickness ($t_{\text{upper}}, t_{\text{lower}}$) is on the order of hundreds of microns. The thermal resistance of condensation in the presence of noncondensable gases (i.e., air) is on the order of $100 \text{ W/m}^2\text{K}^{[3]}$ and the thermal resistance of boiling of fluorocarbon-based fluids is typically on the order of $10,000 \text{ W/m}^2\text{K}^{[4]}$. The measured thermal conductivity of human skin (k_{skin}) varies slightly; we chose

an intermediate value of 3.76 W/m-K.^[5] The thickness of skin (t_{skin}) is on the order of millimeters,^[6,7] varying from 0.7 mm to 5 mm over the human body; an intermediate value of 2 mm was used here, and the temperature beneath the skin was taken as the core internal temperature of the human body, 36 °C.^[8] As shown in Table S2, the thermal resistance of convection heat transfer to the surrounding air dominates the resistance network (it has the highest resistance value); therefore, slight changes in the air conditions (temperature, wind speed, etc.) may result in large changes to the internal temperature under open-loop control. We solved the resistance network over a range of values of h_{air} and T_{air} to demonstrate the sensitivity of an open-loop-controlled STAT to environmental conditions, with the results for the scenario in Figure S18(a) plotted in Figure 3D in the main text and the results for the scenario in Figure S18(b) plotted in Figure S19; the range of h_{air} included in the plot varies from relatively still air up to a noticeable breeze, and the input power is maintained at 3 W. The internal pressure at a given internal temperature, T_{vapor} , is calculated using Equation S5.

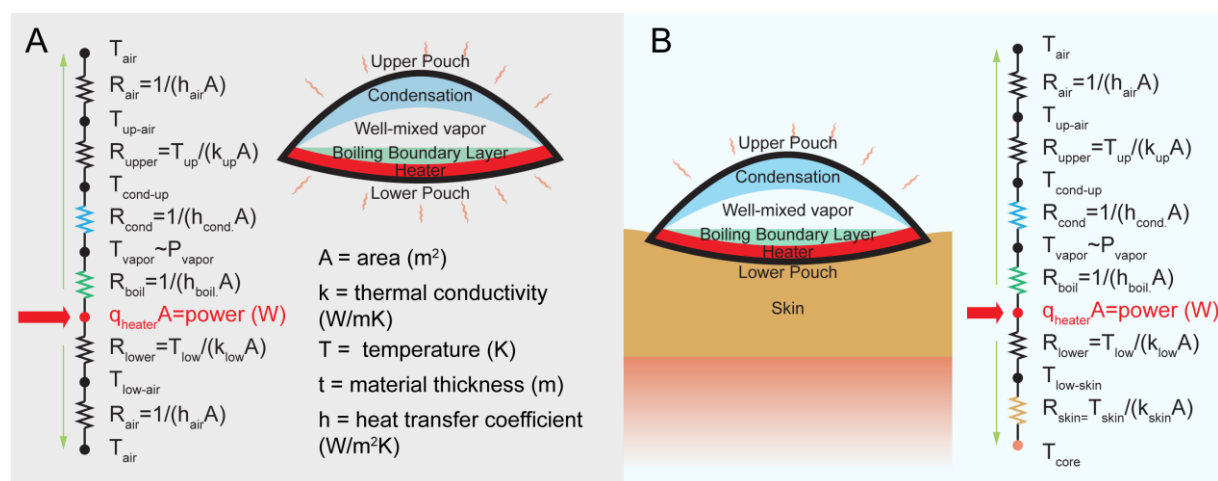


Figure S18. Side-view schematic and corresponding thermal resistance model of a single STAT (A) surrounded by air and (B) adjacent to the human body with one side exposed to air. Heat is generated as electrical current passes through the Joule heater and is dissipated—through the thermal resistance network—to the surroundings.

Table S2. Typical thermal resistance values for STATs, normalized by area, illustrate that the convective heat transfer to the surrounding air presents the greatest resistance to heat transfer.

Quantity	Formula [Variables]	Formula [Values]	Result
R_{air}	$1/h_{\text{air}}$	$1 / [50 \text{ W/m}^2\text{K}]$	$0.02 \text{ m}^2\text{K/W}$
R_{upper}	$t_{\text{upper}}/k_{\text{upper}}$	$0.00015 \text{ m} / [0.25 \text{ W/m-K}]$	$0.0006 \text{ m}^2\text{K/W}$
R_{cond}	$1/h_{\text{cond}}$	$1 / [100 \text{ W/m}^2\text{K}]$	$0.01 \text{ m}^2\text{K/W}$
R_{boil}	$1/h_{\text{boil}}$	$1 / [10,000 \text{ W/m}^2\text{K}]$	$0.0001 \text{ m}^2\text{K/W}$
R_{skin}	$t_{\text{skin}}/k_{\text{skin}}$	$0.002 \text{ m} / [3.76 \text{ W/m-K}]$	$0.0012 \text{ m}^2\text{K/W}$
R_{lower}	$t_{\text{lower}}/k_{\text{lower}}$	$0.0003 \text{ m} / [0.25 \text{ W/m-K}]$	$0.0012 \text{ m}^2\text{K/W}$

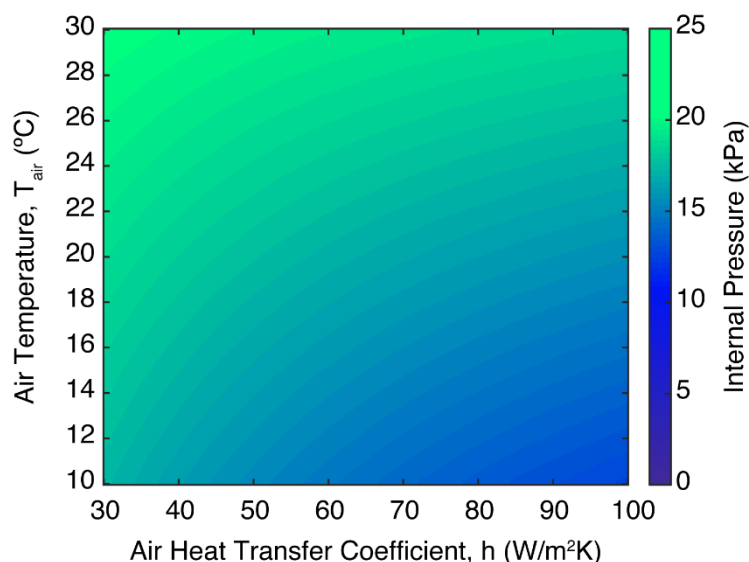


Figure S19. The steady-state open-loop pressure response of a wearable STAT adjacent to the body with a 3 W power input, as predicted from the thermal resistance network shown in Figure S18B, varies significantly as a function of environmental conditions, demonstrating that open-loop control is not a feasible strategy for these thermally-actuated wearables.

5. STAT Lifetime and Closed-Loop Control

To determine the STAT lifetime, we evaluated several durability parameters and evaluated lifetime cycling with closed-loop control. Additionally, we further characterized the environmental effect on closed-loop control.

5.1 STAT Wash-fastness

The water resistance and wash-fastness were studied to evaluate STAT durability for wearable applications. Two 15-line STAT modules were fabricated with soft sensor connections and sealed fastener connections at the heaters. The heater resistance was measured with a multimeter (26III, Fluke Corporation). The baseline sensor capacitance as well as capacitance under applied pressure, where a flat STAT was pressurized with 2.1 kPa using a weighted square indenter placed upon the sensor location, were measured with an LCR meter (380193, Extech Instruments). The STATs were subsequently washed in a home washing machine (WF45R6100AW, Samsung) using settings of “delicate,” temp=1, spin=1, rinse=1, and soil=1 with a commercially available consumer laundry detergent (Tide Free and Gentle, Proctor & Gamble) as used in other studies for its absence of fragrance and dyes (Figure S20A).^[9] Samples were placed in mesh bags during laundering and 727 grams of assorted household textiles were incorporated to meet the minimum load weight. After washing, the samples were air dried and heater resistance and sensor capacitance were measured. This washing test was repeated for 10 cycles, chosen as a benchmark based on the washing durability of the “Google Jacquard Jacket,”^[9,10] a commercially available consumer wearable device that is reported to remain operational for up to 10 machine wash cycles. The normalized capacitance and resistance change are plotted, where C_0 and R_0 are the initial capacitance and initial resistance measurements, respectively (Figure S20B, C, D). Error bars represent combined uncertainty from the measurement device accuracy error and the

statistical variance between three measurements averaged for each data point. Because of the TPU coating, the STATs are inherently water resistant, and STATs exhibit no degradation due to washing. Although STATs are an initial proof of concept, their robustness to washing illustrates they have a care lifetime on par with that of consumer wearables.

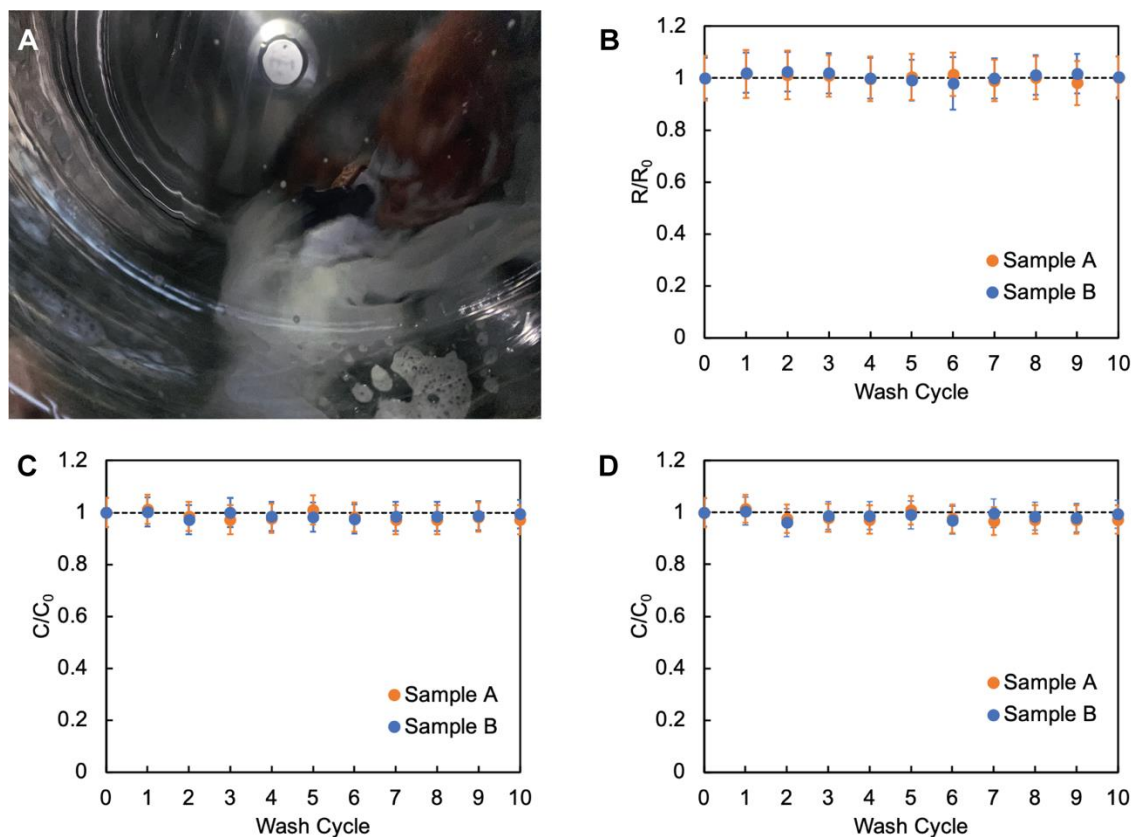


Figure S20. The robustness of STATs to machine washing; photo of STATs in a wash cycle shown in (A). The normalized resistance of the STAT heater (B) and the normalized baseline capacitance (C) and pressurized capacitance (D) of the STAT sensor as a function of wash cycle highlight the absence of statistically significant component degradation after 10 wash cycles.

5.2 STAT Robustness

In order to evaluate STAT robustness to bending, the resilience was studied using one 15-line STAT module with soft sensor connections and fastener connections at the heaters. The STAT was bent manually to a 90° angle (Figure S21A). The heater resistance was measured with a multimeter (26III, Fluke) and the baseline sensor capacitance as well as a pressurized capacitance, where a flat STAT was pressurized with 2.1 kPa using weights at the sensor location, was measured with an LCR meter (380193, Extech). This bending test was repeated for 10,000 cycles of bending, with measurements taken after 1, 10, 100, 1000, and 10,000 cycles. The normalized capacitance and resistance change were plotted, where C_0 and R_0 are the initial capacitance and initial resistance measurements, respectively (Figure S21B, C, D). Error bars represent device accuracy error and measurement error. Because of the flexible nature of the textile materials, the STATs do not exhibit any degradation due to repeated bending.

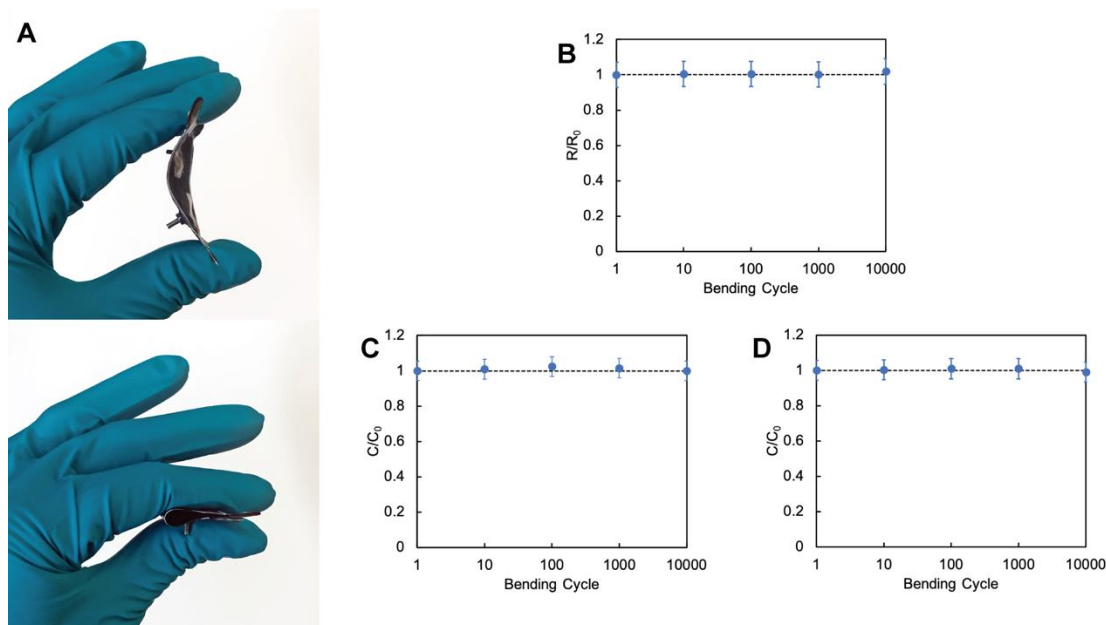


Figure S21. The robustness of STATs to bending, performed as pictured in (A). The normalized resistance of the STAT heater (B) and the normalized baseline capacitance (C) and pressurized capacitance (D) of the STAT sensor as a function of wash cycle highlight that component degradation does not occur during 10,000 cycles of bending.

To further highlight the robustness of STATs, indicative of their long lifetime, a 15-line STAT with soft sensor connections and fastener heater connections and was driven over with a 1605 kg pickup truck (Figure S22). Similarly, due to the compliant nature of the textile and the two-dimensional profile inherent from fabrication, the STAT exhibited no degradation. The heater resistance changed by less than 1%, while the baseline capacitance changed by only 1.5%.



Figure S22. Figure S22. A STAT module being driven over by a 1605 kg pickup truck.

5.3 Closed-Loop Control and Lifetime

The closed-loop control of a module was used to repeatedly regulate pressures. A STAT module with an 11-line heater and fastener-based connections was fabricated. An 11-line heater was chosen for these tests as it has a relatively low resistance (14Ω) which can allow higher powers to be supplied to the system for the purposes of evaluating the closed-loop controller. A total of 0.5 mL of Novec 7000 was injected into the sample, and the sample was then sealed with a minimal amount of residual air. The sensor was calibrated using the method described in the main text.

Single module samples were able to be repeatably actuated for up to 200 cycles, an 80-cycle data set illustrates indicative actuation cycles (Figure S23). The corresponding power input for this dataset is also shown in Figure 4A.

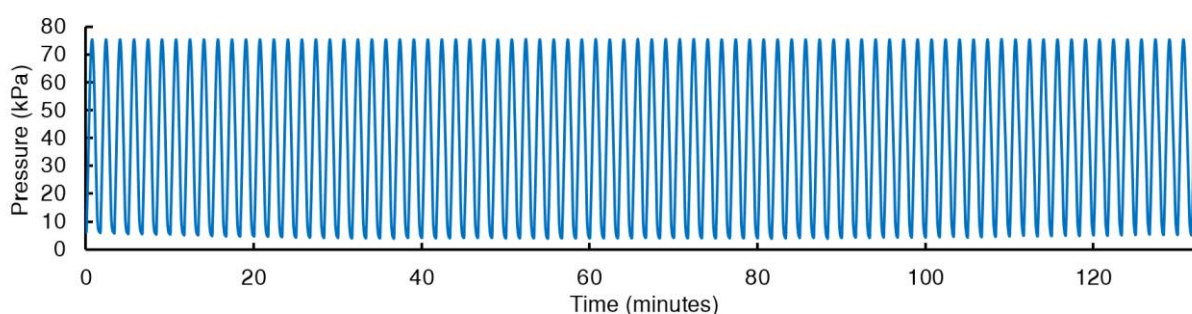


Figure S23. Pressure profile for 80 consecutive cycles of an actuator module with a peak-to-peak sinusoidal command input of 0-75 kPa at an ambient temperature of $10 \text{ }^\circ\text{C}$, at 0.01 Hz

5.4 Environmental Effects on Control

Previous studies illustrated how internal system parameters (such as the power input, heater design, and device orientation) can be set to optimize the system response. This control experiment considers how the external environment can alter the response of the STAT. Cyclic actuation based on a sinusoidal input to the STAT at both hot and cold temperatures was performed. In the room temperature condition, the temperature was monitored using a thermometer and was consistently $22 \text{ }^\circ\text{C}$ throughout the experiment. A temperature-controlled environmental chamber was used to characterize the device in a cooler environment. The environmental temperature was brought to steady state and regulated at $10 \text{ }^\circ\text{C}$. The same module (with 11-line heater and 0.5 mL Novec 7000 working fluid) was used in both characterization tests. The pressure signal from the soft capacitive sensor was acquired by a data acquisition system (Powerlab, AD Instruments). Additionally, a separate analog output from the real-time controller based on the desired pressure input was fed to the data acquisition system, and all data was captured at 1 kHz. Finally, a signal based on the controller output was also acquired by the data acquisition system in order to quantify the instantaneous power input to the heater. Power was estimated based on the known voltage supplied to the controller and known resistance of the heater using both Ohm's law and the electrical power law. Here the STAT can repeatedly achieve the maximum pressure at the programmed timing (Figure S24), while depressurization is inherently limited by environmental conditions without the incorporation of active cooling.

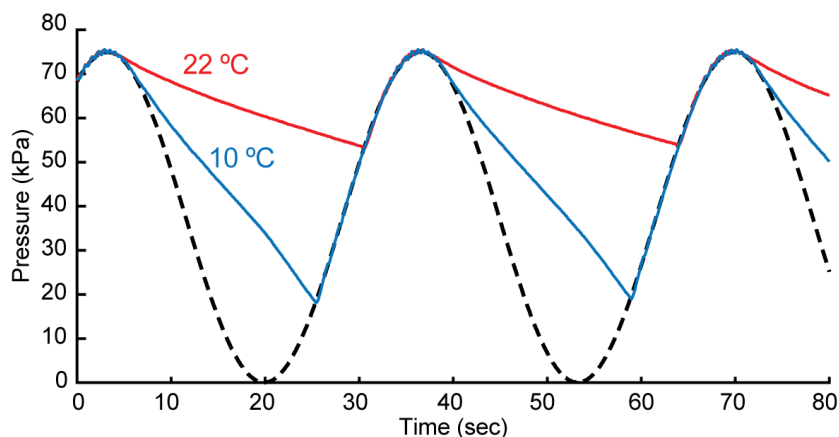


Figure S24. Effects of surrounding environment on the temporal response of a STAT.

The bandwidth of the system was characterized at room temperature conditions and in a cooler environment to demonstrate how the external environment can alter the system dynamics. In this experiment, a frequency sweep was performed across the functioning range of the STAT module at frequencies of 0.002 Hz, 0.005 Hz, 0.01 Hz, 0.02 Hz, 0.03 Hz, 0.05 Hz, 0.08 Hz, 0.1 Hz, 0.2 Hz, 0.3 Hz and 0.5 Hz at room temperature and cooler conditions. The sample was commanded to follow a sinusoidal trajectory from 0-75 kPa. In the room temperature condition, the temperature was monitored using a thermometer and was consistently 22 °C throughout the experiment. A temperature-controlled environmental chamber was used to characterize the device in a cooler environment. The environmental temperature was brought to a steady state at 10 °C. The same module (with 11-line heater and 0.5 mL Novec 7000 working fluid) was used in both characterization tests. The pressure signal from the soft capacitive sensor was acquired by a data acquisition system (Powerlab, AD Instruments). Additionally, a separate analog output from the real-time controller based on the desired pressure input was fed to the data acquisition, and all data was captured at 1 kHz. Finally, a signal based on the controller output was also acquired by the data acquisition system in order to quantify the instantaneous power input to the heater. Power was estimated based on the known voltage supplied to the controller and known resistance of the heater using both Ohm's law and the electrical power law.

Bode plots were generated (Figure S25) based on the peak-to-peak amplitude of the pressure output normalized against the pressure input. Each frequency sweep was repeated three times, and a mean was taken to generate the magnitude values for the Bode plot.

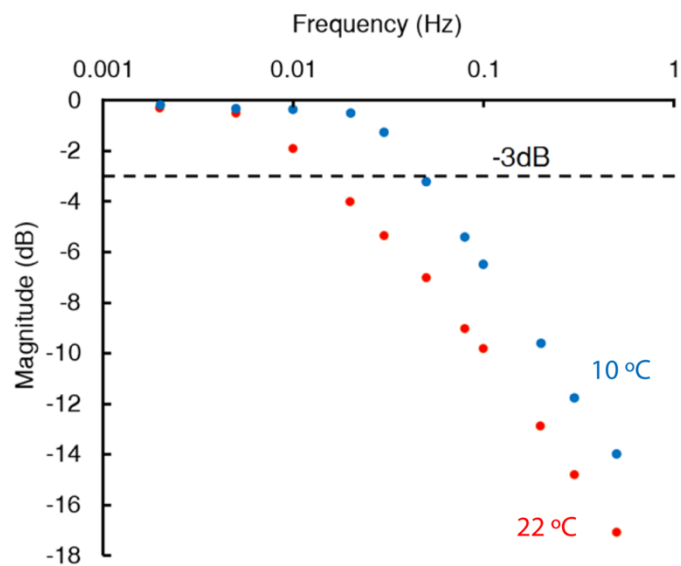


Figure S25. Bode plot of the soft textile module at different environmental conditions.

6. Experimental Section Schematics

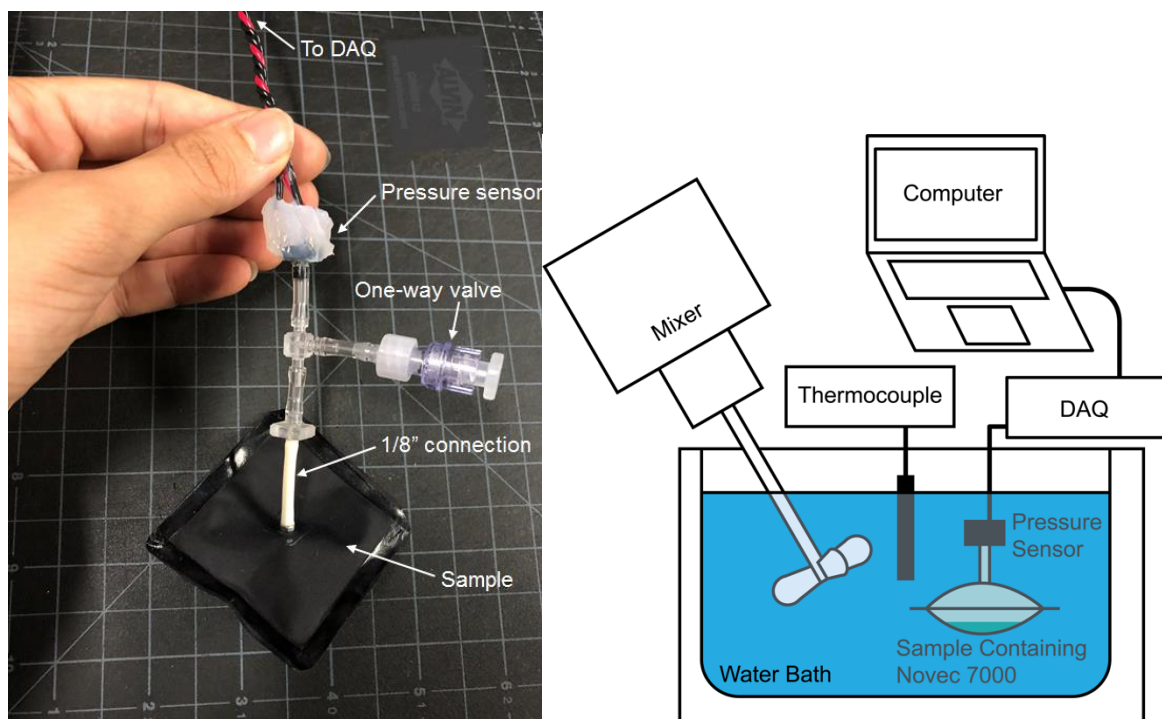


Figure S26. System (left) and setup (right) for steady state temperature-pressure experiment.

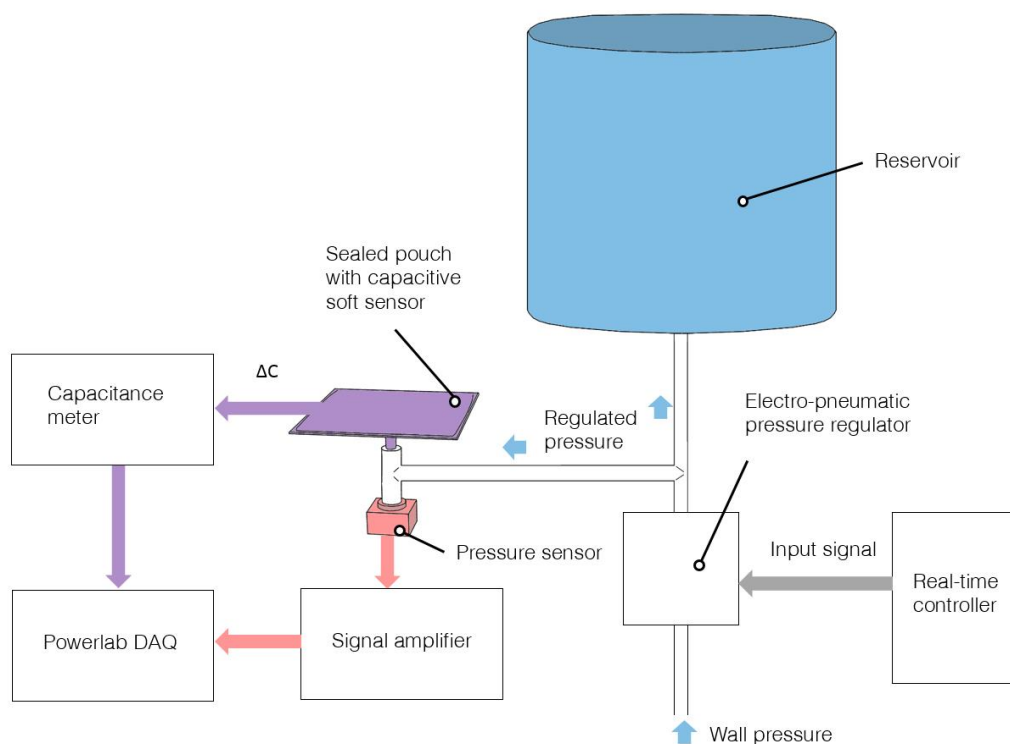


Figure S27. Experimental setup for the capacitance-based soft sensor calibration.

